**Advance Sustainable Science, Engineering and Technology (ASSET)**
**Vol. 8, No.1, January 2026, pp. 02601028-01 ~ 02601028-012**
**ISSN: 2715-4211 DOI:** https://doi.org/10.26877/asset.v8i1.3058

# Effect of NaOH Molarity on Gel Formation at the Geopolymer–Artificial Aggregate Interface for Pavement Applications

**Yayan Adi Saputro[1*], Adnan[2], Gunawan Mohammad[3], Nor Hidayati[1], Nando Nilna Muna[1], Aprilia Citra Ningrum[1]**

[1]Civil Engineering Program Study, Faculty of Science and Technology, Islamic University of Nahdlatul Ulama Jepara, Jepara, Indonesia

[2]Sarhad University of Sains and Information Technology, Peshawar, 25000, Pakistan

[3]Industrial Engineering Program Study, Faculty of Science and Technology, Islamic University of Nahdlatul Ulama Jepara, Jepara, Indonesia

*yayan@unisnu.ac.id

**Abstract**. This study investigates the effect of NaOH molarity (10, 12, and 14 M) on gel formation at the geopolymer–artificial aggregate interfacial transition zone (ITZ) for sustainable pavement binder courses. The study focuses on microstructural and chemical characteristics rather than direct mechanical performance. Using XRF, FTIR, and SEM–EDX analyses, the evolution of gel phases from N-A-S-H to hybrid N/C-A-S-H at the interface was systematically characterized. Increasing NaOH molarity enhanced aluminosilicate dissolution and promoted Ca incorporation, as evidenced by the shift of the main Si–O–T band from approximately 1080 $cm^{-1}$ (10 M) to 960–970 $cm^{-1}$ (14 M) and the increase in Ca/Si ratio from 0.15 to 0.22. Among the investigated mixtures, the 12 M variant exhibited the most homogeneous and compact ITZ microstructure, characterized by a continuous reaction rim, balanced Si/Al (2.96) and Ca/Si (0.22) ratios, and minimal microcracking observed at the microscopic scale.

**Keywords**: geopolymer, interfacial transition zone, alkali activator concentration, hybrid gel formation, artificial aggregate, pavement binder.

***(Received 2025-10-30, Revised 2026-01-13, Accepted 2026-01-15, Available Online by 2026-01-30)***

## 1. Introduction

The need for sustainable and low-carbon construction materials has intensified research exploring substitute binders for ordinary Portland cement, particularly for pavement infrastructure. Conventional OPC production contributes approximately 8% of global $CO_2$ emissions due to the calcination of limestone and high energy consumption in clinker manufacture [1,2]. In this context, Geopolymers have gained recognition as an attractive low-carbon binder alternative. Geopolymers are amorphous to semi-crystalline aluminosilicate materials formed through the alkaline activation of reactive aluminosilicate sources such as fly ash, metakaolin, or slag [1,3,4]. The key binding phases formed during geopolymerization are sodium–alumino–silicate–hydrate (N-A-S-H) and, in the presence of calcium, calcium–(alumino)–silicate–hydrate (C-(A)-S-H) gels or their hybrid combinations (N/C-A-S-H) [5–7]. These gels are responsible for the mechanical strength, dimensional stability, and durability of geopolymeric systems[8–10].

In pavement engineering, the binder–aggregate interfacial transition region critically governs the adhesion, stiffness, and fatigue resistance of the binder course layer[11–13]. While traditional OPC systems depend primarily on C-S-H gel for bonding, geopolymeric binders form more complex chemical interactions at the interface, producing amorphous gel networks that bridge aggregate surfaces [14,15]. The bonding mechanism is thus not only physical but also chemical, involving Si–O–Al and Ca–O–Si linkages that enhance adhesion and interfacial load transfer mechanisms across the interface [14,16]. Recent studies highlight that the morphology and oxide composition of artificial aggregates also influence ITZ performance; optimized aluminosilicate and calcium contents can improve interfacial reactivity and bonding strength [16].

One of the most influential factors determining geopolymer structure and gel composition is the alkaline activator molarity, which controls the dissolution of Si and Al species and the extent of polymerization [17]. Low NaOH molarity often results in incomplete geopolymerization and porous N-A-S-H gels, whereas excessively high molarity may accelerate Ca-rich gel precipitation and induce microcracking due to rapid reaction kinetics and shrinkage[18,19]. Phoo-ngernkham et al. (2018) and Islam et al. (2022) demonstrated that an optimal molar ratio is necessary to balance reactivity and gel densification in alkali-activated materials [18–20]. Furthermore, He et al. (2022) reported the Si/Al ratio yields a denser microstructure and enhances strength performance in geopolymer-based artificial aggregates [17]. These findings indicate that microstructural control through activator composition is critical to improving geopolymer–aggregate adhesion.

Despite these advances, a significant research gap remains concerning the localized identification and transformation of gel phases (from N-A-S-H to C-(A)-S-H) specifically at the geopolymer–artificial aggregate interface relevant to pavement binder courses. Prior investigations mainly focused on bulk strength and phase characterization of geopolymer matrices, with limited emphasis on interfacial-scale chemical evolution and microstructural continuity [12,19,21]. Molecular-level studies have shown that the interfacial bonding between geopolymer binder and aggregates involves hydrogen bonding, Al–O–Si cross-linking, and Na–O coordination, all of which depend on the activator concentration and Ca incorporation [22,23]. However, systematic correlations linking alkaline activator molarity, gel chemistry, and microstructural morphology within the ITZ based on combined SEM, XRF/EDX, and FTIR analyses remain scarce.

To address this gap, the present study investigates the effect of NaOH molarity (10, 12, and 14 M) on the microstructural and chemical bonding characteristics of the geopolymer–artificial aggregate interface. A combination of (FTIR), (XRF), and (SEM–EDX) is employed to identify the gel phases and elemental distribution across the ITZ. The novelty of this work lies in its interface-focused, multi-technique approach that directly correlates oxide composition, vibrational bonding features, and localized microstructural evolution rather than relying solely on bulk geopolymer properties. The results reveal the progressive transformation from N-A-S-H

to hybrid N/C-A-S-H gels with increasing molar ratio and demonstrate that an an intermediate molarity (12 M) promotes a dense and continuous interfacial gel network with balanced Si/Al and Ca/Si ratios and minimal microcracking.

Accordingly, this study is guided by the hypothesis that an intermediate NaOH molarity yields an optimal coexistence of N-A-S-H and C-(A)-S-H gels, resulting in a chemically integrated and microstructurally stable ITZ, whereas lower or higher molarities lead to incomplete polymerization or interfacial instability. This research contributes to a deeper understanding of geopolymer interfacial chemistry and supports the development of sustainable, high-performance materials for road pavement construction.

## 2. Methods

### *2.1. Raw Materials*

The geopolymer binder was synthesized using fly ash sourced from the Tanjung Jati B (Jepara, Indonesia). The alkaline activator solution consisted of a mixture of sodium hydroxide (NaOH) and sodium silicate ($Na_2SiO_3$) solutions. The NaOH solution was prepared by dissolving analytical-grade pellets (≥98% purity) in distilled water and allowed to equilibrate for 24 h prior to mixing to ensure stable molarity and temperature. The sodium silicate solution had a modulus ($SiO_2/Na_2O$) of 3.1, with a solid content of 38–40 wt%.

Artificial coarse aggregates were produced through cold bonding pelletization using geopolymer slurry. These aggregates were designed to have comparable particle size distribution and specific gravity to natural crushed stone (5–10 mm). The binder course matrix was composed of fly ash based geopolymer mortar with fine aggregate (sand) conforming to ASTM C33 gradation [23,24].

### *2.2. Mix Design and Molar Ratio Variation*

Three NaOH molarities (10 M, 12 M, and 14 M) were employed to evaluate the influence of alkaline concentration on gel formation and interfacial characteristics. The $Na_2SiO_3$/NaOH mass ratio was kept constant at 2.5 for all mixtures to isolate the effect of NaOH molarity. The solid-to-liquid (S/L) ratio was fixed at 2.5**,** defined as the mass ratio of total solid precursor (fly ash) to alkaline activator solution. The binder-to-aggregate ratio in the mortar was maintained at 1:2.5 by mass**,** consistent with typical pavement binder course compositions. Each mixture was mechanically mixed for 10 min until a homogeneous paste was achieved and cast into 50 mm cubic molds. For each mix composition, three replicate specimens were prepared to ensure reproducibility.

**Table 1.** Mix Design Parameters of Geopolymer Paste with Artificial Aggregate

| **Parameter** | **MOL 10** | **MOL 12** | **MOL 14** | **Remarks** |
|---|---|---|---|---|
| **Binder type** | Fly ash | Fly ash | Fly ash | Same fly ash source for all mixtures |
| **NaOH molarity (M)** | 10 | 12 | 14 | Main variable of the study |
| **$Na_2SiO_3$/NaOH ratio** | 2,5 | 2,5 | 2,5 | Kept constant |
| **Target Si/Al ratio** | 2.0–2.1 | 2.3–2.4 | 2.6–2.7 | Calculated based on chemical composition |
| **Solid-to-liquid ratio** | 1 : 0.45 | 1 : 0.45 | 1 : 0.45 | Fly ash to alkaline activator solution |

| **Mixture type** | Geopolymer paste | Geopolymer paste | Geopolymer paste | Without coarse aggregate |
|---|---|---|---|---|
| **Binder-to-fine aggregate ratio** | 1 : 2.5 | 1 : 2.5 | 1 : 2.5 | Using fine aggregate |
| **Number of samples per parameter** | 10 | 10 | 10 | Total of 30 samples per mixture |

Each mixture was stirred for 10 min until homogeneous and then poured into 50 mm cubic molds [17], [18]. After casting, all specimens were sealed to prevent moisture loss and cured at ambient laboratory conditions (25 ± 2 °C and relative humidity of 65–75%)**.** Demolding was conducted after 24 h**,** followed by continued curing under the same conditions until testing age. All microstructural and chemical analyses were performed on specimens cured for 28 days**,** ensuring sufficient geopolymerization and gel development prior to characterization.

### *2.3. Preparation of Geopolymer–Aggregate Interface Samples*

To examine the interfacial transition zone (ITZ), artificial aggregate particles were embedded in fresh geopolymer mortar prepared with identical mix proportions. After curing, the hardened specimens were sectioned perpendicular to the binder–aggregate interface using a precision diamond saw. The cut surfaces were polished and carbon-coated prior to SEM–EDX analysis.

### *2.4. X-Ray Fluorescence (XRF) Analysis*

Bulk oxide compositions of both the fly ash precursor and the hardened geopolymer binder were determined using X-Ray Fluorescence (XRF) (PANalytical Axios, wavelength-dispersive spectrometer). Samples were ground to pass a 75 μm sieve and fused with lithium tetraborate flux. Each composition was analyzed in duplicate to verify consistency and average oxide values were used to calculate Si/Al and Ca/Si ratios as indicators of dominant gel types. The obtained oxide composition was used to calculate Si/Al and Ca/Si ratios, which are essential indicators of gel type dominance (N-A-S-H vs. C-(A)-S-H) [13,20].

### *2.5. Fourier Transform Infrared Spectroscopy (FTIR)*

FTIR spectra were recorded using a PerkinElmer Spectrum Two spectrometer within the range of 4000–400 $cm^{-1}$ at a resolution of 4 $cm^{-1}$, averaging 32 scans per sample. The powdered geopolymer samples (≤63 μm) were mixed with KBr (1:100 ratio) and pressed into transparent pellets. For each NaOH molarity, two independent measurements were conducted to confirm spectral reproducibility. Peak shifts were interpreted qualitatively to assess changes in aluminosilicate polymerization..

### *2.6. Scanning Electron Microscopy and Energy Dispersive X-ray Spectroscopy (SEM–EDX)*

SEM–EDX analyses were performed using a JEOL JSM-IT500 microscope operated at 15 kV with a working distance of 10 mm. Backscattered electron imaging was used to enhance compositional contrast across the ITZ. For each specimen, at least five representative EDX spot analyses were conducted within the ITZ and three spots in the bulk matrix, and average elemental ratios (Si/Al and Ca/Si) were reported to minimize local heterogeneity effects. Variability among measurements was assessed qualitatively by comparing trends across replicate specimens rather than relying on single-point analyses.

### *2.7. Analytical Approach and Data Reliability*

The combined results of XRF, FTIR, and SEM–EDX were used to establish correlations among oxide composition, gel type, and microstructural morphology. Although no direct mechanical or interfacial performance tests were conducted, data reliability was ensured through replicate specimen preparation, repeated measurements, and consistent trends observed across all

characterization techniques. This integrated approach provides a robust qualitative assessment of how NaOH molarity governs gel evolution at the geopolymer–artificial aggregate interface.

## 3. Results and Discussion

### *3.1. Komposisi oksida bulk - XRF*

XRF analysis provides the mass oxide composition (%) for the artificial aggregate (AB) and geopolymer samples MOL 10, MOL 12, and MOL 14. The bulk oxide composition results are as shown in Figure 1 below :

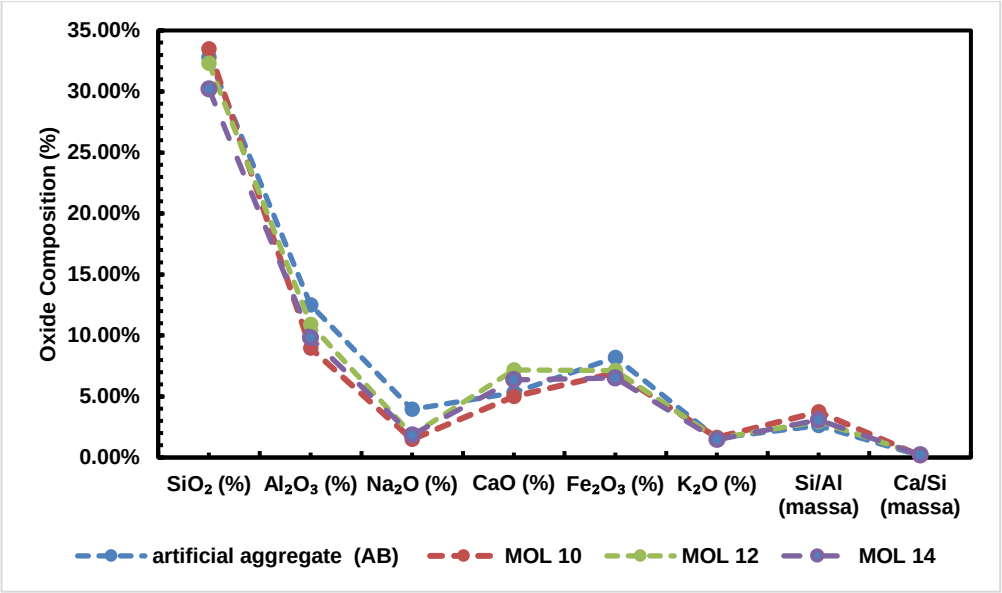


**Figure 1.** Bulk Oxide Composition

The oxide compositions of the fly ash–based geopolymer binder and artificial aggregate were determined by XRF (Table 3). The artificial aggregate (AB) contained 32.8% $SiO_2$, 12.5% $Al_2O_3$, and 5.3% CaO, resulting in a Si/Al ratio of 2.62 and Ca/Si ratio of 0.16. In contrast, the geopolymer matrices exhibited compositional variations with increasing molar ratios (MOL 10, MOL 12, and MOL 14). At MOL 10, the binder contained 33.5% $SiO_2$ and 4.99% CaO, giving a Si/Al of 3.74 and Ca/Si of 0.15. At MOL 12, CaO increased to 7.18% while Si/Al decreased to 2.96 indicating enhanced Ca incorporation and greater Al substitution within the aluminosilicate network. At MOL 14, $SiO_2$ decreased slightly (30.2%) with CaO 6.37%, maintaining a Ca/Si ratio near 0.21. These quantitative trends demonstrate that NaOH molarity governs bulk chemical availability for gel formation, with MOL 12 providing a balanced Si–Al–Ca composition conducive to hybrid gel development. XRF measurements confirmed consistent compositional trends across all mixtures. The moderate Ca enrichment at MOL 12 reflects a favorable balance between geopolymerization and secondary hydration, consistent with the coexistence of N-A-S-H and C-(A)-S-H gels [25–27].

### *3.2. FTIR results identification of key bands and shift of Si–O–T bands*

From the spectrum results (4000–400 $cm^{-1}$) in the sample, there are dominant bands around as in Figure 2 below :

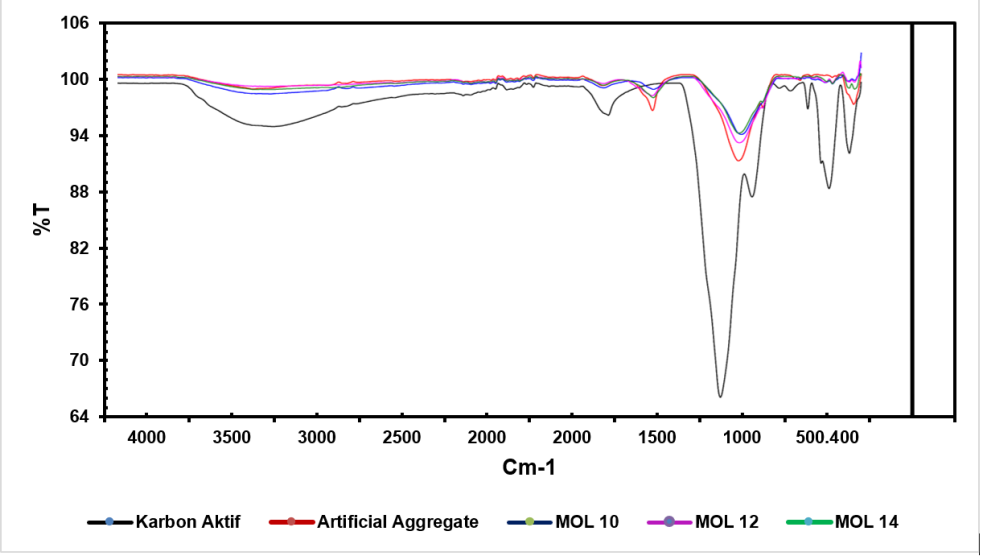


**Figure 2.** Spectrum Results (4000–400 $Cm^{-1}$)

Overall, the FTIR spectrum shows the typical characteristics of geopolymer materials with a dominant band in the 900–1100 $cm^{-1}$ region which confirms the formation of aluminosilicate bonds (N–A–S–H or (N,C)–A–S–H gel). The presence of –OH and H–O–H bands indicates that the sample still contains bound water which contributes to the mechanical properties and microstructure.

**Table 2.** FTIR Characteristic Bands of Geopolymer Binders (MOL 10–14)

| No | Peak position ($cm^{-1}$) | General interpretation | Information |
|---|---|---|---|
| **1** | ~3238 | O–H stretching (air/gel struktural) | Indicates the presence of bound water in the geopolymer gel. |
| **2** | ~1620 | H–O–H bending vibration | Molecular water or light hydration |
| **3** | ~1080 | Asymmetric Si–O–T (T = Si/Al) stretching | The main peak of geopolymer gel formation |
| **4** | ~927 | Si–O–Al vibration | Strong indication of N-A-S-H formation |
| **5** | ~742 – 657 | Si–O bending / quartz atau feldspar residual | Aggregate non-reactive phase |
| **6** | ~555 – 457 | Al–O dan Si–O–Si bending | Amorphous aluminosilicate network |

**Table 3.** Peak shift analysis between MOLs by comparing the main peaks of Si–O–T (~1080 $cm^{-1}$):

| Sampel | Main position ($cm^{-1}$) | Interpretation |
|---|---|---|
| **MOL 10** | ~1080 | The structure is still similar to the initial silicate source, the reaction is not yet optimal. |
| **MOL 12** | ~1010 – 1000 (diperkirakan dari pola spektrum gabungan) | Shift to lower wave numbers → Al substitution increases → formation of dominant N-A-S-H gel |
| **MOL 14** | ~970 – 950 | Further shift → indicates further polymerization & emergence of Ca-rich phase (C-(A)-S-H) due to high alkali and Ca ratio of artificial aggregates |

FTIR spectra of the geopolymer samples revealed distinct vibrational changes in the Si–O–T (T = Si or Al) framework, as summarized in Figure 5. The main asymmetric stretching band for Si–O–T shifted systematically toward lower wavenumbers as the molar ratio increased:

- MOL 10: main band at ≈1080 $cm^{-1}$, characteristic of unreacted silicate or early N-A-S-H gel.
- MOL 12: shifted to ≈1000–1010 $cm^{-1}$, indicating enhanced Al substitution and formation of a more polymerized aluminosilicate network.
- MOL 14: further shifted to ≈960–970 $cm^{-1}$, attributed to the incorporation of Ca into the geopolymer matrix and formation of hybrid N/C-A-S-H gel.

Broad O–H stretching at 3230–3400 $cm^{-1}$ and H–O–H bending around 1630 $cm^{-1}$ were detected in all samples, reflecting bound water and hydrated gel phases. Minor bands near 1420–1450 $cm^{-1}$ correspond to carbonate stretching, suggesting limited atmospheric carbonation[21].

The progressive shift of the Si–O–T band from ~1080 to ~960 $cm^{-1}$ with increasing molar ratio is a strong indicator of polymerization progression and gel transformation. This trend confirms that higher alkalinity enhances dissolution and reorganization of the aluminosilicate network, while the appearance of Ca–O–Si linkages at MOL 12–14 marks the onset of C-(A)-S-H formation [28–30].

### *3.3. SEM observation (interface morphology) - 500×*

SEM micrographs at 500× magnification (Figure 3) clearly illustrate the morphological evolution of the binder–aggregate interface with molar ratio variation.

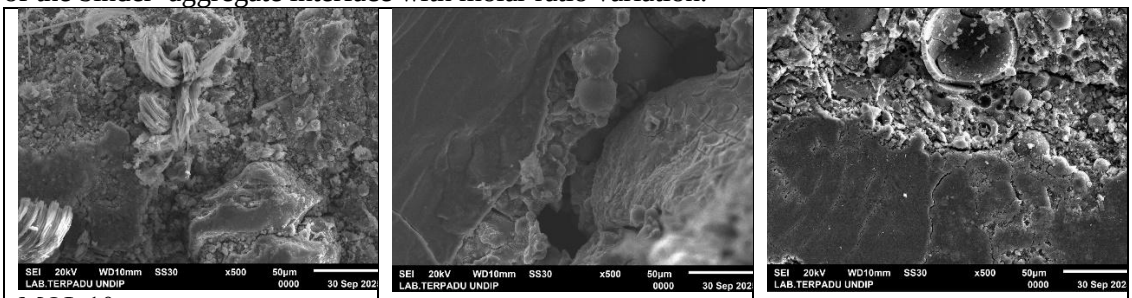


| MOL 10 | MOL 12 | MOL 14 |
|---|---|---|

**Figure 3.** SEM observation (interface morphology) **-**500×

MOL 10 exhibited a porous, granular microstructure with a discontinuous reaction rim and visible interfacial gaps between binder and aggregate. The surface appears rough and heterogeneous, indicating incomplete geopolymerization and limited bonding. MOL 12 presented a dense, compact matrix with a continuous reaction rim tightly adhering to the aggregate surface. The interfacial transition zone (ITZ) was well integrated and largely free of microvoids, demonstrating enhanced chemical bonding. MOL 14 displayed a fully densified structure with smoother gel phases and few open pores, yet local shrinkage cracks were observed near the ITZ, suggesting microstructural stress due to rapid polymerization and water loss.

The morphological transition from porous to dense ITZ across the molar series aligns with chemical data, signifying that MOL 12 achieves the most balanced interfacial densification. The excessive densification at MOL 14, although beneficial for mechanical strength, may increase the risk of microcracking under thermal or drying conditions [31,32]

### *3.4. SEM–EDX — local composition in the ITZ (spot & oxide analysis)*

SEM–EDX spot analyses at the interface confirm compositional variations consistent with gel evolution (Table 4).

**Table 4.** *SEM–EDX — local composition in the ITZ (spot & oxide analysis)*

| Sample | $Na_2O$ (wt%) | $Al_2O_3$ (wt%) | $SiO_2$ (wt%) | CaO (wt%) | FeO (wt%) | Interpretation |
|---|---|---|---|---|---|---|

| | | | | | | |
|---|---|---|---|---|---|---|
| **MOL 10** | 12.99 | 14.97 | 40.02 | 5.35 | 4.24 | Na–Al–Si-rich surface; N-A-S-H dominant |
| **MOL 12** | 12.60 | 8.74 | 40.97 | 5.73 | 8.01 | Balanced Na–Si–Ca composition; mixed N-A-S-H / C-(A)-S-H |
| **MOL 14** | 6.13 | 12.17 | 42.53 | 10.41 | 9.16 | Ca-enriched region; C-(A)-S-H / hybrid gel dominant |

At MOL 10, the high $Na_2O$ and $Al_2O_3$ contents suggest the presence of a sodium aluminosilicate network typical of N-A-S-H gels. The CaO content (5.35 wt%) remains relatively low, consistent with limited Ca participation. MOL 12 displays a more balanced composition, with moderate CaO (5.73 wt%) and uniform $SiO_2$ distribution, confirming the coexistence of N-A-S-H and C-(A)-S-H phases at the ITZ. MOL 14 shows significant Ca enrichment (10.41 wt%), indicative of a dominant C-(A)-S-H phase and hybrid gel formation.

The increasing Ca/Si ratio across the samples (from ~0.15 in MOL 10 to ~0.22 in MOL 12 and ~0.21 in MOL 14) mirrors the observed FTIR shifts and XRF results, confirming that gel chemistry transitions from Na–Al–Si to Ca–Si-based structures as alkalinity increases [33–35]

*3.5. Integration: XRF ↔ FTIR ↔ SEM–EDX correlation (gel formation mechanism in ITZ)*

The integrated findings from XRF, FTIR, SEM, and EDX collectively describe the transformation mechanism of the geopolymer–aggregate interface:

1. MOL 10: High Si/Al (3.74), low Ca/Si (0.15), FTIR at 1080 $cm^{-1}$, and porous ITZ morphology indicate a sodium aluminosilicate gel (N-A-S-H) with limited polymerization. The interface bonding is primarily physical with minimal chemical continuity.
2. MOL 12: Si/Al reduced (2.96), Ca/Si increased (0.22), FTIR shift to ~1000 $cm^{-1}$, and formation of a continuous reaction rim reveal a mixed gel structure combining N-A-S-H and C-(A)-S-H. This balanced composition yields the densest and most chemically integrated interface.
3. MOL 14: High CaO (10.41 wt%), strong FTIR shift (~960 $cm^{-1}$), and microcrack development confirm the dominance of Ca-rich hybrid gels (N/C-A-S-H). Excess alkalinity accelerates reaction kinetics, leading to local stress and potential shrinkage.

These observations validate that the molar ratio plays a pivotal role in governing the microstructure and chemistry of the ITZ, determining the extent of polymerization and hybrid gel formation. Optimal interface densification occurs at MOL 12, where simultaneous geopolymerization and calcium incorporation yield a cohesive microstructure without excessive brittleness.

3.6. Technical implications for road pavement binder course

From a pavement materials perspective, the geopolymer–artificial aggregate system with MOL 12 demonstrates the most promising microstructural characteristics. The continuous and dense ITZ promotes superior load transfer and improved fatigue resistance, essential for binder course layers subjected to repetitive traffic loads. The excessive Ca-rich phase at MOL 14, though beneficial for early strength, may introduce micro-shrinkage or durability concerns under field curing conditions. Thus, moderate alkalinity (MOL 12) is recommended to achieve a balanced N-A-S-H / C-(A)-S-H network, combining adequate strength with microstructural stability. These findings align with Figure 4. Los Angeles Abrasion

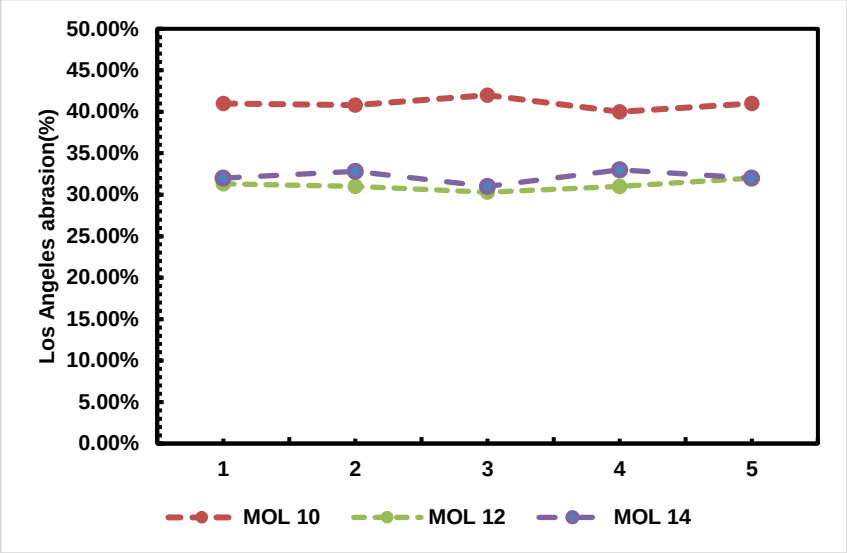


**Figure 4.** Los Angeles Abrasion

Based on the average values obtained from five samples, MOL 10 shows the highest Los Angeles abrasion loss (40.96%), indicating lower resistance to abrasion. This result suggests that the geopolymer matrix formed at 10 M NaOH is not sufficiently dense to withstand mechanical wear. The lowest abrasion loss is observed for MOL 12, with an average value of 31.12%. The consistent results across all samples indicate that 12 M NaOH provides an optimum activator concentration, leading to better geopolymerization and improved aggregate durability. For MOL 14, the average abrasion loss slightly increases to 32.16%. Although higher alkalinity enhances geopolymerization, excessive NaOH concentration may negatively affect the internal structure of the aggregates, resulting in a minor reduction in abrasion resistance compared to MOL 12. Overall, the results show that abrasion resistance improves with increasing NaOH molarity up to 12 M, after which a slight decline occurs. Both MOL 12 and MOL 14 meet the general abrasion requirement for pavement aggregates (≤40%), while MOL 10 approaches the limit. These findings align with prior studies on alkali-activated pavements where intermediate activator concentrations provided optimal adhesion and long-term performance [36,37].

## 4. Conclusion

This study evaluated the effect of NaOH molarity (10 M, 12 M, and 14 M) on gel formation and interfacial microstructure at the geopolymer–artificial aggregate interface. Direct microstructural and chemical analyses (XRF, FTIR, and SEM–EDX) showed that increasing molarity enhanced aluminosilicate dissolution and calcium incorporation, leading to a transition from N-A-S-H-dominated gels to hybrid N/C-A-S-H structures. Among the investigated mixtures, the 12 M system exhibited the most balanced ITZ, characterized by a dense and continuous reaction rim with intermediate Si/Al and Ca/Si ratios and minimal microcracking. The compact and chemically integrated ITZ observed at 12 M is considered a favorable prerequisite for binder–aggregate interaction in pavement binder course materials.

**Acknowledgements**

The authors sincerely appreciate the financial support granted by Kemendiktisaintek through the Fundamental Research Grant Scheme (Fundamental) 2025. The research facilities and technical assistance made available by Universitas Islam Nahdlatul Ulama (UNISNU) Jepara were invaluable to the completion of this study. The contributions from laboratory staff and technical personnel who assisted in sample preparation and testing are gratefully acknowledged. Their support significantly enhanced the quality and successful execution of this research.

**References**


[1] Davidovits J. Geopolymer Chemistry and Applications. vol. 171. 2008.

[2] Duxson P, Fernández-Jiménez A, Provis J, Lukey G, Palomo A, Van Deventer J. Geopolymer Technology: The Current State of the Art. J Mater Sci 2007;42:2917–33. https://doi.org/10.1007/s10853-006-0637-z.

[3] San Nicolas R, Provis J. The Interfacial Transition Zone in Alkali-Activated Slag Mortars. Front Mater 2015;2. https://doi.org/10.3389/fmats.2015.00070.

[4] Nath P, Sarker PK. Effect of GGBFS on setting, workability and early strength properties of fly ash geopolymer concrete cured in ambient condition. Constr Build Mater 2014;66:163–71. https://doi.org/https://doi.org/10.1016/j.conbuildmat.2014.05.080.

[5] Fernández-Jiménez A, Palomo A. Composition and Microstructure of Alkali Activated Fly Ash Binder. Cement and Concrete Research 2005;35:1984–92. https://doi.org/10.1016/j.cemconres.2005.03.003.

[6] Lee NK, Lee HK. Setting and mechanical properties of alkali-activated fly ash/slag concrete manufactured at room temperature. Construction and Building Materials 2013;47:1201–9. https://doi.org/https://doi.org/10.1016/j.conbuildmat.2013.05.107.

[7] Matsuda A, Maruyama I, Meawad A, Araki Y. Reaction, Phases, and Microstructure of Fly Ash-Based Alkali-Activated Materials. Journal of Advanced Concrete Technology 2019;17:93–101. https://doi.org/10.3151/jact.17.93.

[8] Thomas M. Supplementary Cementing Materials in Concrete. 2013. https://doi.org/10.1201/b14493.

[9] Guo X, Shi H, Dick W. Compressive strength and microstructural characteristics of class C fly ash geopolymer. Cement and Concrete Composites 2010;32:142–7. https://doi.org/10.1016/j.cemconcomp.2009.11.003.

[10] Sharmin S. The microstructural characterization of alkali- activated binders incorporating waste clay brick powder with fly ash and GGBFS 2025. https://doi.org/10.1080/21650373.2025.2586659.

[11] Singh B, Ishwarya G, Gupta M, Bhattacharyya SK. Geopolymer concrete: A review of some recent developments. Construction and Building Materials 2015;85:78–90. https://doi.org/https://doi.org/10.1016/j.conbuildmat.2015.03.036.

[12] Peng H, Cui C, Cai CS, Liu Y, Liu Z. Microstructure and microhardness property of the interface between a metakaolin/GGBFS-based geopolymer paste and granite aggregate. Construction and Building Materials 2019;221:263–73. https://doi.org/10.1016/j.conbuildmat.2019.06.090.

[13] Techniques I. Geopolymer-Based Artificial Aggregates : A Review on Methods 2022.

[14] Kai M, Dai J-G. Understanding geopolymer binder-aggregate interfacial characteristics at molecular level. Cement and Concrete Research 2021;149:106582. https://doi.org/10.1016/j.cemconres.2021.106582.

[15] Komnitsas K, Soultana A, Bartzas G. Marble Waste Valorization through Alkali Activation 2021.

[16] Yip CK, Lukey GC, van Deventer JSJ. The coexistence of geopolymeric gel and calcium silicate hydrate at the early stage of alkaline activation. Cem Concr Res 2005;35:1688–97. https://doi.org/https://doi.org/10.1016/j.cemconres.2004.10.042.

[17] Ahmad Sofri L, Abdullah MMAB, Mohd Hasan MR, Huang Y. The Influence of Sodium Hydroxide Concentration on Physical Properties and Strength Development of High Calcium Fly Ash Based Geopolymer as Pavement Base Materials. IOP Conf Ser Mater Sci Eng 2020;864:12016. https://doi.org/10.1088/1757-899X/864/1/012016.

[18] Mishra A, Choudhary D, Jain N, Kumar M, Sharda N, Dutt D. Effect of concentration of alkali liquid and curing time on strength and water absorption of geopolymer concrete. Journal of Engineering and Applied Science 2008;3.
[19] Nath S, Maitra S, Mukherjee S, Kumar S. Microstructural evolution of fly ash geopolymer: effect of alkali concentration. 2015.
[20] Khale D, Chaudhary R. Mechanism of geopolymerization and factors influencing its development: A review. Journal of Materials Science 2007;42:729–46. https://doi.org/10.1007/s10853-006-0401-4.
[21] Fu Q, Bu M, Zhang Z, Xu W, Yuan Q, Niu D. Hydration Characteristics and Microstructure of Alkali-Activated Slag Concrete: A Review. Engineering 2023;20:162–79. https://doi.org/https://doi.org/10.1016/j.eng.2021.07.026.
[22] Asif A, Man Z, Khairun Azizi A, Nuruddin M, Ismail L. The Effect of Si/Al Ratio and Sodium Silicate on the Mechanical Properties of Fly Ash Based Geopolymer for Coating. Materials Science Forum 2014;803:355–61. https://doi.org/10.4028/www.scientific.net/MSF.803.355.
[23] Saputro YA, Widagdo J, Arifin S, Assa'idi S, Miftahunnajah NAP, Bon AT. Setting time and compressive strength of geopolymer concrete with variations in the addition of cement. AIP Conference Proceedings 2024.
[24] Saputro YA, Mudiyono R, Antonius. The analysis of mortar concrete with the variety of sands in jepara (keling sand, bangsri sand) using strong pressure method. Journal of Physics: Conference Series 2019;1363. https://doi.org/10.1088/1742-6596/1363/1/012089.
[25] Wong CL, Yap SP, Alengaram UJ, Yuen CW, Yeo JS, Mo KH. Properties of high calcium fly ash geopolymer incorporating recycled brick waste and borax. Hybrid Advances 2024;5:100130. https://doi.org/https://doi.org/10.1016/j.hybadv.2023.100130.
[26] Jitchaiyaphum K, Suksiripattanapong C. Enhancement of Properties of Fly Ash Geopolymer Paste with Low NaOH Concentrations Using a Pressing Approach 2025:186–99.
[27] Nuaklong P, Wongsa A, Sata V, Boonserm K, Sanjayan J, Chindaprasirt P. Properties of high-calcium and low-calcium fly ash combination geopolymer mortar containing recycled aggregate. Heliyon 2019;5:e02513. https://doi.org/https://doi.org/10.1016/j.heliyon.2019.e02513.
[28] Wong CL, Yap SP, Alengaram UJ, Yuen CW, Yeo JS, Mo KH. Properties of high calcium fly ash geopolymer incorporating recycled brick waste and borax. Hybrid Advances 2024;5:100130. https://doi.org/https://doi.org/10.1016/j.hybadv.2023.100130.
[29] Poojalakshmi ES, Nagarajan P, Sudhakumar J, Thomas BS. Impact of alkaline activator concentration on mechanical properties and microstructure of a ternary blended one-part geopolymer cement. Sci Rep 2025;15:33808. https://doi.org/10.1038/s41598-025-01610-1.
[30] Wang J, Hu Z, Chen Y, Huang J, Ma Y, Zhu W, et al. Effect of Ca/Si and Al/Si on micromechanical properties of C(-A)-S-H. Cem Concr Res 2022;157:106811. https://doi.org/https://doi.org/10.1016/j.cemconres.2022.106811.
[31] Luo Y, Koh CH, Li SH, Brouwers HJH, Yu Q. Understanding the thermal behavior of geopolymeric composites designed by packing model. Cem Concr Compos 2023;143:105265. https://doi.org/https://doi.org/10.1016/j.cemconcomp.2023.105265.
[32] Sajan P, Jiang T, Lau C, Tan G, Ng K. Combined effect of curing temperature, curing period and alkaline concentration on the mechanical properties of fly ash-based geopolymer. Cleaner Materials 2021;1:100002. https://doi.org/https://doi.org/10.1016/j.clema.2021.100002.

[33] Yip CK, Lukey GC, van Deventer JSJ. The coexistence of geopolymeric gel and calcium silicate hydrate at the early stage of alkaline activation. Cem Concr Res 2005;35:1688–97. https://doi.org/https://doi.org/10.1016/j.cemconres.2004.10.042.

[34] El Alouani M, Saufi H, Aouan B, Bassam R, Alehyen S, Rachdi Y, et al. A comprehensive review of synthesis, characterization, and applications of aluminosilicate materials-based geopolymers. Environmental Advances 2024;16:100524. https://doi.org/https://doi.org/10.1016/j.envadv.2024.100524.

[35] Madirisha MM, Dada OR, Ikotun BD. Chemical fundamentals of geopolymers in sustainable construction. Materials Today Sustainability 2024;27:100842. https://doi.org/https://doi.org/10.1016/j.mtsust.2024.100842.

[36] Nanda RP, Priya N. Geopolymer as stabilising materials in pavement constructions: A review. Cleaner Waste Systems 2024;7:100134. https://doi.org/https://doi.org/10.1016/j.clwas.2024.100134.

[37] Shilar FA, Ganachari S V, Patil VB, Khan TMY, Javed S, Baig RU. Optimization of Alkaline Activator on the Strength Properties of Geopolymer Concrete. Polymers (Basel) 2022;14. https://doi.org/10.3390/polym14122434.